Early Prediction of Glaucoma Disease with a Hybrid S-CIELAB - Based Smoothing Spatial Filter and Fast Fourier Transform

Anita Madona M[1], Panneer Arokiaraj S[2]

[1]Research Scholar, Department of Computer Science, Thanthai Periyar Govt. Arts and Science College (Autonomous), Affiliated to Bharathidasan University, Tiruchirappalli, India
madonaphd[at]gmail.com

[2]Associate Professor, Department of Computer Science, Thanthai Periyar Govt. Arts and Science College (Autonomous), Affiliated to Bharathidasan University Tiruchirappalli, India
drpancs[at]gmail.com

Abstract: ***This paper develops an image analysis algorithm to help with glaucomatous eyes' cup-to-disc ratio calculation. The method depends on color data, color discrepancies among neighboring frames, and the shape of the regions. It also takes into consideration the specialist's viewing preferences. This technique is used to separate the Optic Disc (OD) into the fundus image in Glaucomatous Eyes (GE) and the Optic Cup (OC) inside the OD. SS-CIELAB uses several spatial smoothing filters to simulate the contrast sensitivity features of the Human Vision System (HVS) in the color space of the adversary. To create the sharpened image, they combine these spatial filters with each opponent channel's Fast Fourier Transform (FFT). The application created to separate the OD and OC is meant to help with estimating the cup-to-disc ratio in GE. A technique that depends on the color data and the color differences among neighboring pixels and the shape of the regions in the assertion. The researcher makes use of the color image sharpening method and incorporates the spatial filter ring provided by the S-CIELAB module.***

Keywords: Glaucomatous Eyes; Spatial Filters; Fast Fourier Transform; Optic Cup; S-CIELAB

1. Introduction

An important international standard for determining color reproduction mistakes would be the CIELAB system. This technique was developed at a time when the majority of color-reproduction programs focused on matching big, uniform-colored areas [1-2]. As a result, data from color-appearance assessments of sizable uniform fields were used to test the CIELAB system. Many programs have been created to process actual photographs as a result of the development of digital color imaging [3]. Many psychophysical experiments have demonstrated that the appearance and discrimination of finely patterned or small-field colors vary from comparable assessments done using vast uniform fields [4]. CIELAB does not produce good results when used to forecast local color reproduction problems in patterned images. A point-by-point estimation of the CIELAB error for instance results in substantial inaccuracies at most image points when they combine a continuous-tone color image of a halftone version of the image [5]. Since the halftone patterns shift quickly, the eye cannot distinguish these variances, thus the copy could still maintain the original's appearance.

Glaucoma was a severe and irreversible neurodegenerative eye illness that develops when the Optic Nerve Head (ONH) of the eye was damaged as a result of elevated intraocular pressure. Permanent blindness is the outcome after it slowly degrades ONH [6]. Early glaucoma identification could prevent the ONH from suffering further damage. 76 million people worldwide would suffer from glaucoma by 2020. A recent development in the study of medical images is the Computer-Aided Diagnosis (CAD) of glaucoma [7]. The CAD has gained popularity as a more precise tool for glaucoma defection due to recent advancements in image processing techniques and fast computers. Since it is quicker, more affordable, and more accurate, glaucoma detection with CAD may someday become a well-organized technique [8]. The CDR assessment along with other medical exams including the Intraocular Pressure (IOP) and visual field test was crucial for appropriately assessing glaucoma in patients.

2. Related Works

The CDR was measured manually by ophthalmologists in the current convention [9]. This heavily contributes to the ability and experience of the ophthalmologist, and modifications regarding the spectators can also be peculiar. Early glaucoma detection is essential for a successful medical invention because manual CDR assessment and use are not feasible for mass screening [10]. Since multiple vascular groups cross the ocular cup's border, the automatic CDR measurement, optic papilla, and segmentation present a challenging aspect [11]. As a result, when thresholding techniques have been used the precision of the retrieved features was impacted.

The examination and detection of some retinal components, OD the excavation, & vascular groups or arteries located inside it serve as the starting point for glaucoma research [12]. Measurements of CDR and Neuro Retinal Rim (NRR) thickness are the characteristics that are most frequently examined. OD and OC Separation were challenging of currently utilized artificial glaucoma diagnosis algorithms [13]. Segmentation is a very important step in an automatic analysis that ultimately controls the accuracy of results [14]. Blood vessels in the OD of the current application affect image segmentation. The exposure of potential excavations and the precise optic disc contour are also impacted by this challenge [15]. Despite this, many attested outcomes for the identification of glaucoma are dependent on CDR.

A mathematical morphology should only be used to segment a color fundus image to diagnose glaucoma. Researchers have divided the optic papilla & ocular cup into sections as they work to process the CDR proportion [16]. The contour model's established methods, including the Hough Transform, Fuzzy Convergence, Template Matching, and geometric parametric model, are used to determine the papilla exposure [17]. An elliptical fitting method was used to evaluate CDR values. K-means clustering was used iteratively to identify the optic papilla and ocular cup region [18]. To achieve region growth put on the optic papilla, confinement uses Fast Fourier change established pattern matching. This approach then uses this information in the span creating a method with the purpose of segmentation [19].

It could have a reduction in the number of professionals needed and a shorter examination period as its key benefits [20].To this goal, we take into account individual retinal images taken by a non-mydriatic camera [21]. TA method relies on color information, color differences among nearby pixels, and the shape of the problem areas.

3. Proposed System

The proposed architecture consists of the following steps is shown in Figure 1 and the explanation given below;

3.1 Datasets Used

200 retinal images from several databases, including DRION, DRISHTI, STARE, HRF, and local datasets, and photos chosen at random from glaucoma-specialized ophthalmologists' earlier selections from a larger collection of images were used to assess the proposed method. Images were extracted from several datasets so that it could be verified that the suggested methodology operates under varied imaging situations, such as different sizes, resolutions, and lighting conditions [22]. Images were chosen at random to demonstrate the clarity of the research's key areas in the following ratio: 12:12:7: 1:8.

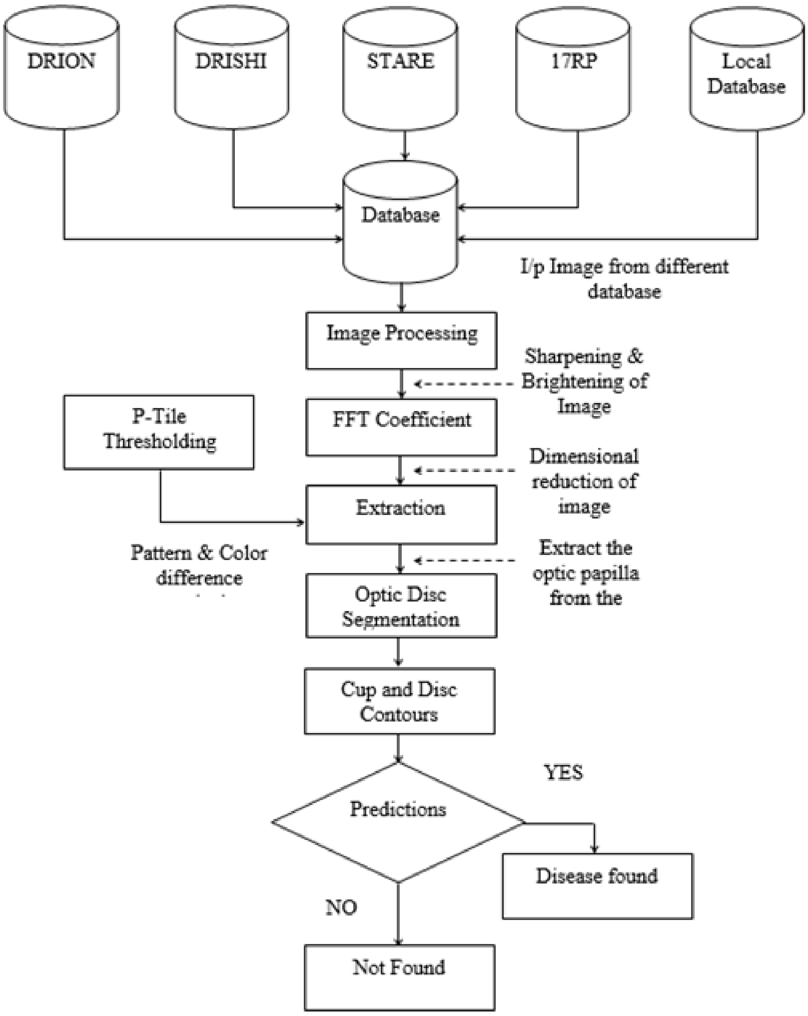

Figure 1: Overall Architecture for Proposed Model

3.2 Image Preprocessing

S-CIELAB uses several smoothing spatial filters to simulate the contrast sensitivity mechanisms of the HVS in the color space of the adversary. Linear combinations of Gaussian masses make up the spatial filters. Our technique for sharpening color images combines S-CIELAB, incorporates the adversarial color space and derivative edge detectors, and viewing variables & HVS. The input images are just sequentially translated for device independence from the RGB color area to the CIEXYZ color representation, and then to the adversary color image. An expression could theoretically be used to describe the sharpened image ShI_x displays.

$$ShI_x(i,j) = I_x(i,j) - kLoG[F_{dx}] * I_x(i,j) \tag{1}$$

where $I_x(i,j)$ was its area of interest in the input image, i=0,1,2 is the color channel of the adversary, and k is the sharpening depth. j connected to the viewing distances and the ppi value shown to the device. A sharpened image of the monitor was interpreted as a smoothed, spatially filtered version when viewed from a specific distance. According to the equation, the projected sharpened image ShI_x can be used to generate the perceived sharpened image ShI_{dx} by convolving with the spatial filters.

$$ShI_{dx}(i,j) = F_{dx}(i,j) * ShI_x(i,j) \tag{2}$$

In this work, we take into account an RGB display with 100 PPI, which equates to d=35 pixels/degree and two sharpening depths of k=5 & k=1. To separate the OD, we pick a deeper sharpness, and to separate the cup, a lighter one.

We must select 3 spatial filters and color transformations to specify the S-CIELAB transformation. The filters & transformation determined to people's psychophysical measures of color presentation were used in the computations below. The CIE 1931 XYZ tristimulus values are used to specify the input image, which is then converted into 3 opponent-color planes that represent the brightness, blue-yellow & red-greenimage. A linear conversion of opponent colors to XYZ was

$$Op = 0.2797 + 0.727 - 0.I07Z \ (3)$$
$$O; = -0.449X + 0.29Y - 0077Z \ (4)$$
$$O3 = 0.086€ - 0.597 + 0.501Z \ (5)$$

Data in each plane was filtered using spatial kernels that may be separated into two dimensions.

$$f = k\sum w_x E_x \tag{6}$$

Where,

$$E_x = k_x exp(-(x+y)^2/\sigma_x^2) \tag{7}$$

The scaling factor k; is selected in the discrete implementation that E_x values to 1. The linear function was selected such that the two-dimensional kernel of each color plane is shown in Table 1.

Table 1: 3 color planes have the following characteristics:

Plane	Weights w'/	Spreads
Lum	0.923 0.106 -0.110	0.029 0.135 4.41
Red-green	0.533 0.332	0.0391 0.495
Blue-yellow	0.489 0.372	0.0537 0.389

where the spread denotes the degree of the viewing angle.

Researchers can integrate S-CIELAB as a preprocessing to currently existing CIELAB-associated hardware & software because the spatial processing stage was distinct from the CIELAB computation. The spatial extension could be easily applied to various color-difference investigations because the pattern and color phases may be distinguished.

3.3 FFT Coefficients

Shift-invariant global frequency information can be found in the frequency spectrum. Authors make use of the FFT coefficients' genuine response. The response to a feature ffft∈ R30 was compressed during a dimension reduction through PCA. The high-dimensional image data is converted into a compressed but accurate feature vector f using a dimension reduction approach like PCA. The authors converted the 2-dimensional preprocessed images, P ∈ R128×128 to an image vector, p ∈ R128.128. An implicit computation of the eigenvectors from the learning set's images produced the decomposition matrix. Thirty major components were utilized for further classification because our earlier research demonstrated that they already cover at least 95% of the data variation. Raw pixel intensities are used to create the feature vector, which is represented by fraw∈ R30.OD localization on the green plane uses single or seed points. Fourier transform and P-Tile thresholding are combined to extract ROI. The image is separated into sin and cosine components using the Fourier transform, which is represented by Equation (8).

$$C_{n} = \frac{1}{T}\int_{-\frac{T}{2}}^{\frac{T}{2}} f(I)\, e^{-2\pi x\left(\frac{n}{T}\right)i}\, di \tag{8}$$

Equation (9) shows that the Fourier coefficients Cn obtain in the parameter rapidly decrease when n is any integer. As a result, the uniform and absolute forms of f(x) converge.

3.4 Extraction

P-Tile thresholding was employed because it necessitates the understanding of the size of items seen in the image [23]. Inside the image, it separates the interesting area. Equation 3 states that h(c,d) was considered as 0 if the score of the criterion is determined to be greater than it, otherwise it is treated as 1. P-Tile thresholding was mathematically expressed by the following condition.

$$If\ h(c,d) > T\ then\ h(c,d) = 0\ else\ h(c,d) = 255 \tag{9}$$

The red plane represents an image with the highest intensity; hence the image is converted to the red plane. Figure 2 below shows the extracted ROI.

Figure 2: Red Plane ROI Extraction.

3.5 Optic Disk Segmentation

A retinal fundus image has a lot of arteries and veins, therefore vascular groups must be removed to properly extract the optic papilla from the image. Vascular groups are removed using morphological opening and closing procedures and a flat disc structuring element with a diameter of 6 pixels, which was determined by using the biggest blood vessel thickness in the normalized image as a reference. Equations (4) and (5) can be used to express the morphological opening and closing processes, correspondingly, while Figures3 (a) and (b) shows a graphical representation of these morphological actions on a fundus image.

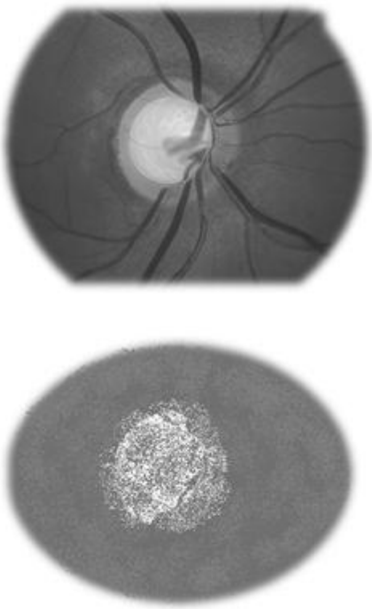

Figure 3: (a) ROI and **(b)** Opening/Closing

The segmentation of the optical disc region is then accomplished by combining Active Contour and Circular Hough Transform. For boundary identification in the image, the Hough transform extracts circles from the faulty input image. After applying to open and shutting methods, the blood vessels in Figures 2(a) and 2(b) are removed from the image. Figure 2(b) shows the retrieved vessel-free image, whose mask was properly generated from the optic papilla boundary using the Circular Hough Transform.

3.6 Cup and Disc Contours

Several factors influence how the NRR outer contour was determined. Retinal arteries and veins cut across it rather than appear to be a continuous shape. This forces our algorithm to make an educated guess regarding the obstructed regions of the NRR contour. A basic color scheme that they apply to the area of interest is shown in Figure 4(a) was predicated on the color distinctions among neighboring pixels. Since the optic disc is nearly round-shaped, a new image was created in polar coordinates. The authors only focus on the band in Figure 4 (b) that is constrained by the blue areas because the image's center and corners are uninteresting for our goal of determining the rim contour. The center of the artery and temporal side are scarce and the difference between the NRR and the remainder of the EFs—in terms of CIEDE2000 color difference - is greatest and corresponds to the top and bottom files of this novel array. Finally going to predict the disease found or not.

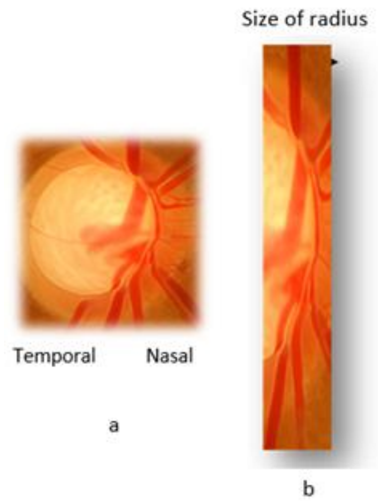

Figure 4: (a) Radius **(b)** Threshold

4. Results and Discussion

JPEG-DCT halftone images, compressed images, and a few straightforward assessment patterns were used to evaluate S-CIELAB. Three opposing-color planes of an image are transformed using the JPEG-DCT, as seen in Figure 5. This image is made using the common JPEG-DCT compression process with a quality function group of 75, making the compressed image barely distinguishable from the original. The brightness plane is fuzzier at this level of compression. The calculations presented in the paper will employ the averaged regionally filtration version ShI_{dx} of Figure 6, which viewer would see under the visual experience specified by dx.

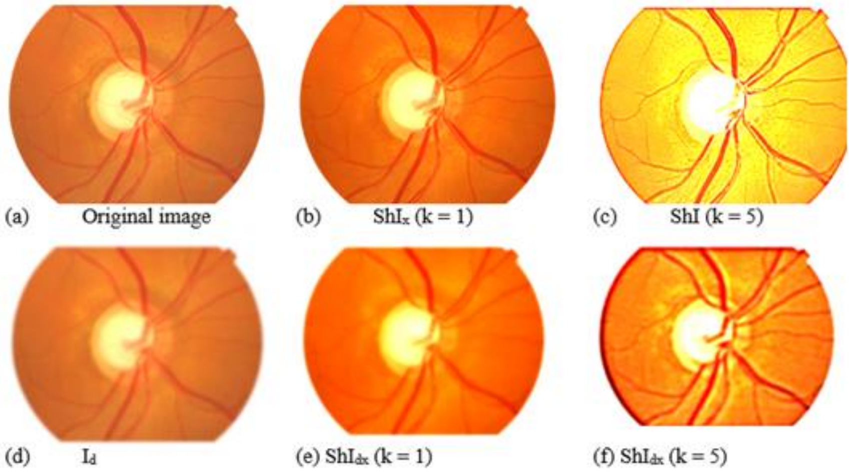

Figures 5: (a)-(c) display the sharpened and original versions of the images and spatially filtered images in (d)–(f)

Figure 5 contrasts the condensed image's CIELAB and S-CIELAB replication mistakes. The solid line depicts how the AE values were distributed throughout the original and compacted images after being evaluated point-by-point through CIELAB. According to the cIELAB error distribution of AE values, 36% of the image had AE values greater than 5 units and 10% had AE values greater than 10 units. Color discrepancies of this scale are obvious to relate to the color accuracy of large regular fields, although very few inaccuracies are noticeable. These AE values, therefore, exceed the perceived difference.

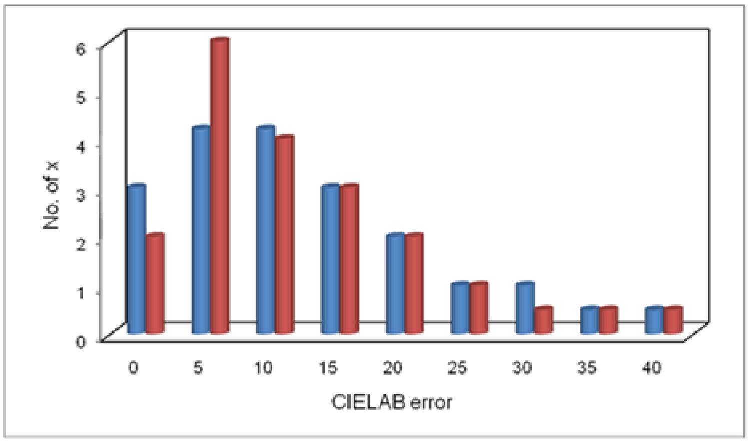

Figure 6: Distributions of the CIELAB

4.1 Effect of Viewing Distance

The effect of viewing distance on the segmentation of the OD and OC after using the segmentation method on the supposedly brightened image of the retina fundus. Researchers have used the S-CIELAB-based technique for color image sharpening. We have taken into account viewing the sharpened image with a resolution of 100 dpi at various distances L=25, 50, and 100 cm from the monitor. The outcomes are displayed in Figure 7 (a). The results obtained for the OC and disc contours in Figure 7 (a) have been duplicated on original versions of the image and displayed in Figure 7 (b) for comparative purposes.

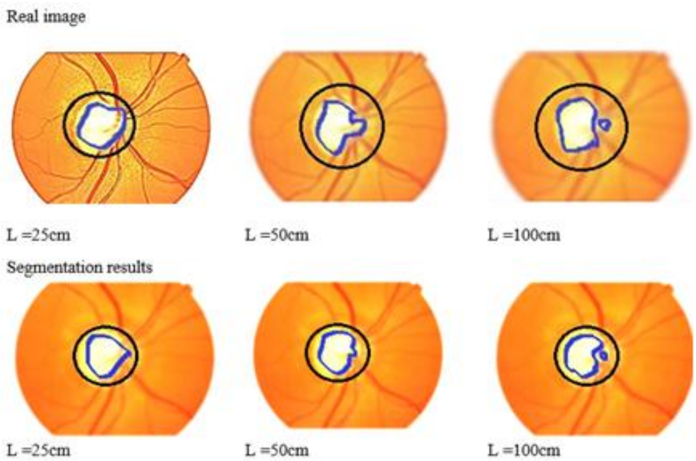

Paper ID: SR25210222137 DOI: https://dx.doi.org/10.21275/SR25210222137

International Journal of Science and Research (IJSR)
ISSN: 2319-7064
Impact Factor 2024: 7.101

Figure 7: The sharpened color images segment the OD and OC

As shown in Figure 7(a), the contour of the optical cup varies dramatically with viewing distance because minute details and color variances in the image that better depict the contour of the optical cup cannot be recognized at long distances. As opposed to this, changes in viewing distance have less of an impact on the shape of the optic disc. Figure 8 displays many original optic disc images along with the outcomes obtained by using the proposed algorithm. Several scenarios involving dynamic range, contrast, and noise level between the disc and the fundus are displayed. The OD is divided by a blue line and the cup by a red line. Although the separation of the cup needs development to challenging circumstances, overall, the results are adequate.

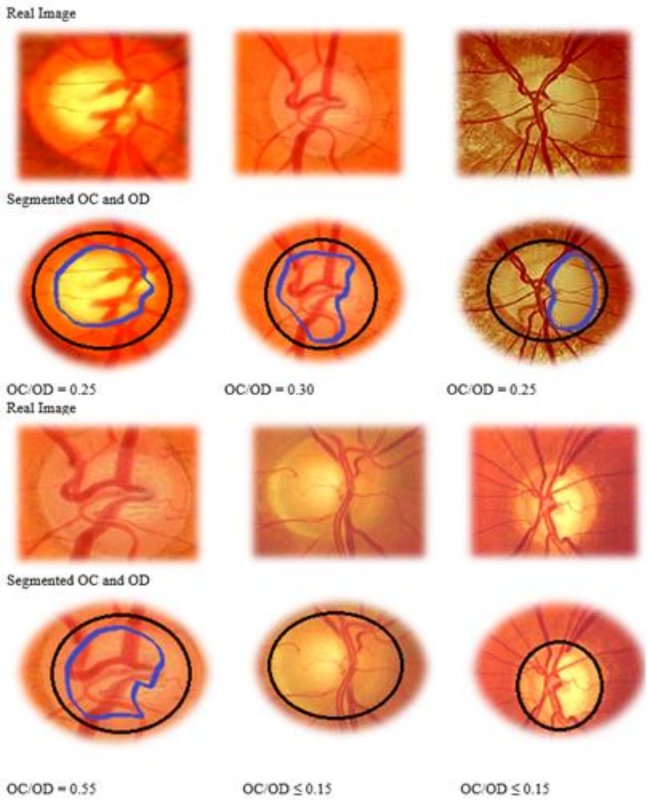

Figure 8: Outcomes

As a consequence of this data analysis, we can observe that the procedure should only be applied at viewing distances between 2550cm and 3000cm. Researchers exhibit the CIEDE2000 color difference ΔE00, the Luminance ΔL, the Chroma ΔC, and the Hue ΔH differences, in that order, computed for the pixels of the image's first row in polar coordinates in Figure 7 to demonstrate the impact of the viewing conditions on the sharpened image to segment. In comparison to the remaining plots that correspond to larger distances, the maxima could be found more easily in the plots corresponding to viewing distances of L=25 cm and L=50 cm. The maxima of the Figure 9ΔC plot could be discussed similarly.

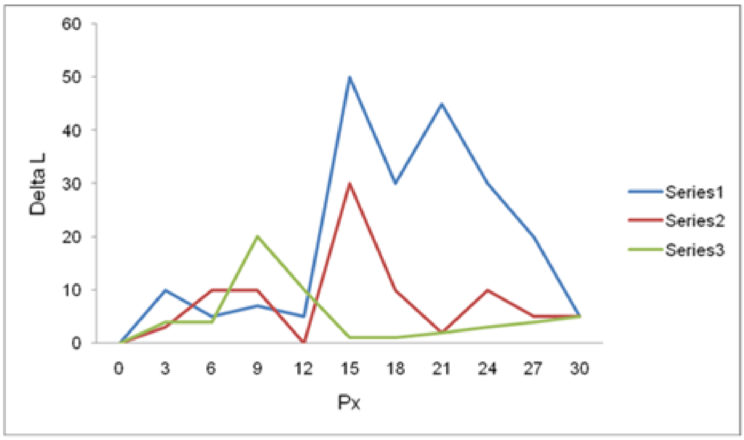

Figure 9: Polar-coordinated image

Enhancing fundus images is hardly understood in the context of glaucoma detection. Due to the presence of numerous retinal diseases hemorrhages, vascular groups, microaneurysms, and exudates, it is exceedingly difficult to precisely define the ocular cup & optic papilla. Furthermore, the exact assessment of the optic disc boundary is very difficult because of the modest fundus image variation. For subsequent processing, the improvement approach makes use of the green channel plane. The extraction of ROI makes use of the Fourier transform and P-Tile thresholding. Feature extraction is the most often used method for glaucoma detection are proven ones. Optic papilla and ocular cup are extracted as features using Active Contour Model and Circular Hough Transform. Combining these two different feature types can result in higher ideal resolutions for glaucoma identification.

To determine the optic papilla and ocular cup portions, a recursive Active Contour model and Circular Hough transform are used at the extracted ROI. To pinpoint the ocular cup and optic disc locations, the elliptical fitting method is then used on the image. Using P-Tile thresholding, the artery found inside the OD is isolated, and the ISNT rule is used to apply four distinct masks to assess the thickness of the NRR. When RDR is determined, glaucoma is detected if the p-value is more than 0.01. The faster glaucoma progresses, the lower the value of RDR and the higher the value of CDR. The proposed methodology's efficacy was evaluated using various datasets, and the features, such as CDR, RDR, Mean, Standard Deviation, and p-value proportions, are automatically calculated by measuring the thickness of NRR in the inferior, superior, nasal, and temporal quadrants, or ISNT quadrants.

4.2 Comparison with Proposed Methodology

Results of the suggested technique applied to 200 photographs of actual patients are shown in Table 2, demonstrating its sensitivity, specificity, and accuracy. 153 of these 200 photos were thought to be related to glaucoma, while 47 were normal.

Table 2: The soft system technique's outcomes

Diagnosis	Results
True Positive	152
False Positive	3
True Negative	47
False Negative	4
Sensitivity	99%
Specificity	96%
Accuracy	98.2%

Table 2 displays the findings of other additional techniques for detecting progressive glaucoma. The newly proposed technique is compared to CDR measurement characteristics, such as the sensitivity and specificity of current methods. 98% sensitivity and 97.5% specificity were demonstrated by the suggested approach.

Table 3: Comparison of existing and proposed system

Investigation type	Sensitivity	Specificity
Two fully connected layer CNN [21]	97.9%-100%	86%-99.4%
EfficientDet-D0 with EfficientNet-B0 [14]	88%	86%
Generalized Deep Learning [22]	81%-91%	55%-76%
Disc-Aware Ensemble Network [16]	61	82%-94.9%
Cup Disc Ratio [13][17]	x%0-95%	46%-82.1%
Proposed method	18.8%-81.5%	97.7%
	99%	

5. Conclusions

A collection of genuine images taken with a non-mydriatic retinal camera have been used to test the techniques for the automatic segmentation of the OC and OD to the nerve head. They are designed to help eye care professionals to estimate the cup-to-disc ratio, a crucial variable for identifying glaucoma risk. The methods are based on an examination of the color disparities between neighboring pixels and the color content of the region. The optic disc boundary's smoothness and rounded form have been taken into account. On 200 photos, the suggested algorithm was evaluated. In 195 photos, it was discovered that the procedure was successful, achieving 95% specificity, 98% sensitivity, and 97.5% accuracy. The results show that the proposed methodology is efficient and applicable to the development of new medical structures for the correct automatic detection and recognition of glaucoma.

References

[1] Thakur, N., &Juneja, M. (2021). Pre-processing of retinal images for removal of outliers. Wireless Personal Communications, 116, 739-765.
[2] Ayub, J., Ahmad, J., Muhammad, J., Aziz, L., Ayub, S., Akram, U., &Basit, I. (2016, April). Glaucoma detection through the optic disc and cup segmentation using K-mean clustering. In 2016 international conference on computing, electronic and electrical engineering (ICE Cube) (pp. 143-147). IEEE.
[3] Anantrasirichai, N., Nicholson, L., Morgan, J. E., Erchova, I., &Achim, A. (2013, September). Adaptive-weighted bilateral filtering for optical coherence tomography. In 2013 IEEE International Conference on Image Processing (pp. 1110-1114). IEEE.
[4] Anantrasirichai, N., Nicholson, L., Morgan, J. E., Erchova, I., Mortlock, K., North, R. V., ... &Achim, A.

(2014). Adaptive-weighted bilateral filtering and other pre-processing techniques for optical coherence tomography. Computerized Medical Imaging and Graphics, 38(6), 526-539.

[5] Srinivasu, P. N., Rao, T. S., Srinivas, G., & Reddy, P. V. G. D. (2020). A computationally efficient skull scraping approach for brain MR image. Recent Advances in Computer Science and Communications (Formerly: Recent Patents on Computer Science), 13(5), 833-844.

[6] Hasan, M. J., Alom, M. S., Fatema, U., & Wahid, M. F. (2021, July). Deep Learning Based Retinal OCT Image Denoising using Generative Adversarial Network. In 2021 International Conference on Automation, Control and Mechatronics for Industry 4.0 (ACMI) (pp. 1-6). IEEE.

[7] Latchoumi TP, Swathi R, Vidyasri P, Balamurugan K. Develop New Algorithm To Improve Safety On WMSN In Health Disease Monitoring. In2022 International Mobile and Embedded Technology Conference (MECON) 2022 Mar 10 (pp. 357-362). IEEE.

[8] Villamizar, J., Calderón, G., Carrillo, J., Bautista Rozo, L., Carrillo, J., Rueda, J., & Castillo, J. (2022). Mimetic finite difference methods for restoration of fundus images for automatic detection of glaucoma suspects. Computer methods in biomechanics and biomedical engineering: imaging & visualization, 10(5), 492-499.

[9] Lazaridis, G., Lorenzi, M., Ourselin, S., &Garway-Heath, D. (2019). Enhancing OCT signal by fusion of GANs: improving statistical power of glaucoma clinical trials. In Medical Image Computing and Computer Assisted Intervention–MICCAI 2019: 22nd International Conference, Shenzhen, China, October 13–17, 2019, Proceedings, Part I 22 (pp. 3-11). Springer International Publishing.

[10] Tulsani, A., Kumar, P., &Pathan, S. (2021). Automated segmentation of optic disc and optic cup for glaucoma assessment using improved UNET++ architecture. Biocybernetics and Biomedical Engineering, 41(2), 819-832.

[11] Sahu, S., Singh, H. V., Kumar, B., Singh, A. K., & Kumar, P. (2019). Image processing based automated glaucoma detection techniques and role of de-noising: a technical survey. Handbook of Multimedia Information Security: Techniques and Applications, 359-375.

[12] Santosh, N. K., &Barpanda, S. S. (2022). Wavelet and PCA-based glaucoma classification through novel methodological enhanced retinal images. Machine Vision and Applications, 33(1), 11.

[13] Garikapati PR, Balamurugan K, Latchoumi TP, Shankar G. A Quantitative Study of Small Dataset Machining by Agglomerative Hierarchical Cluster and K-Medoid. InEmergent Converging Technologies and Biomedical Systems 2022 (pp. 717-727). Springer, Singapore.

[14] Kandavalli, M. A., Yuvaraj, C. R., &Nandini Devi, M. S. (2019). Performance Evaluation of Various Filtering Techniques for Retinal Fundus Images. Indian Journal of Public Health Research & Development, 10(11).

[15] Haider, A., Arsalan, M., Lee, M. B., Owais, M., Mahmood, T., Sultan, H., & Park, K. R. (2022). Artificial Intelligence-based computer-aided diagnosis of glaucoma using retinal fundus images. Expert Systems with Applications, 207, 117968.

[16] Shinde, R. (2021). Glaucoma detection in retinal fundus images using U-Net and supervised machine learning algorithms. Intelligence-Based Medicine, 5, 100038.

[17] Anand, S. G. G. S. S., Gayathri, S., &Sangeethapriya, G. (2022). Optic disc analysis in retinal fundus using L 2 norm of contourletsubbands, superimposed edges, and morphological filling. Multimedia Tools and Applications, 1-24.

[18] Bautista, L., Villamizar, J., Calderón, G., Carrillo E, J. C., Rueda, J. C., & Castillo, J. (2019). Mimetic Finite Difference Methods for Restoration of Fundus Images for Automatic Glaucoma Detection. In VipIMAGE 2019: Proceedings of the VII ECCOMAS Thematic Conference on Computational Vision and Medical Image Processing, October 16–18, 2019, Porto, Portugal (pp. 104-113). Springer International Publishing.

[19] Elseid, A. A. G., & Hamza, A. O. (2019). Glaucoma detection using retinal nerve fiber layer texture features. Journal of Clinical Engineering, 44(4), 180-185.

[20] Ganesh, S. S., Kannayeram, G., Karthick, A., & Muhibbullah, M. (2021). A novel context-aware joint segmentation and classification framework for glaucoma detection. Computational and Mathematical Methods in Medicine, 2021.

[21] Singh, L. K., Garg, H., Khanna, M., &Bhadoria, R. S. (2021). An enhanced deep image model for glaucoma diagnosis using feature-based detection in the retinal fundus. Medical & Biological Engineering & Computing, 59, 333-353.

[22] Bowd, C., Belghith, A., Rezapour, J., Christopher, M., Hyman, L., Jonas, J. B., ... & Zangwill, L. M. (2022). Diagnostic Accuracy of Macular Thickness Map and Texture En Face Images for Detecting Glaucoma in Eyes with Axial High Myopia. American Journal of Ophthalmology, 242, 26-35.

[23] Singh, L. K., &Garg, H. (2020). Automated glaucoma-type identification using machine learning or deep learning techniques. Advancement of machine intelligence in interactive medical image analysis, 241-263.